COMMUNICATIONS PHYSICS

ARTICLE

https://doi.org/10.1038/s42005-020-00426-x OPEN

Work function seen with sub-meV precision through laser photoemission

Y. Ishida[1,2✉], J. K. Jung[1,3], M. S. Kim[1,3], J. Kwon[1,3], Y. S. Kim[1,3], D. Chung[4], I. Song[1,3], C. Kim[1,3], T. Otsu[2] & Y. Kobayashi[2]

Electron emission can be utilised to measure the work function of the surface. However, the number of significant digits in the values obtained through thermionic-, field- and photo-emission techniques is typically just two or three. Here, we show that the number can go up to five when angle-resolved photoemission spectroscopy (ARPES) is applied. This owes to the capability of ARPES to detect the slowest photoelectrons that are directed only along the surface normal. By using a laser-based source, we optimised our setup for the slow photo-electrons and resolved the slowest-end cutoff of Au(111) with the sharpness not deteriorated by the bandwidth of light nor by Fermi-Dirac distribution. The work function was leveled within ±0.4 meV at least from 30 to 90 K and the surface aging was discerned as a meV shift of the work function. Our study opens the investigations into the fifth significant digit of the work function.

[1] Center for Correlated Electron Systems, Institute for Basic Science, Seoul 08826, Republic of Korea. [2] ISSP, The University of Tokyo, Kashiwa, Chiba 277-8581, Japan. [3] Department of Physics and Astronomy, Seoul National University, Seoul 08826, Republic of Korea. [4] College of Liberal Studies, Seoul National University, Seoul 08826, Republic of Korea. ✉email: ishiday@issp.u-tokyo.ac.jp

Among the electronic properties of a crystal surface, the work function (ϕ_s) is one of the fundamentals. It corresponds to the minimum energy required to take out an electron through the surface at 0 K[1,2]. The values of ϕ_s serve as a test bench for the theory of surface electronic structures[3–6] and are relevant to a variety of electronic and chemical phenomena on surfaces and interfaces. The topics include the junction-device behaviours, charge-carrier injection and surface catalytic interactions[7–9].

Electrons emitted from a crystal can be utilised to measure ϕ_s directly because the threshold of the emission is governed by ϕ_s which acts as a potential barrier on the surface. Thus, thermionic-, field- and photo-emission techniques have been applied to this end[1]. However, the thresholds are not as sharp as naively expected, and the experimental values of ϕ_s typically have just two or three significant digits[1]. This number is also typical to other techniques; see Kawano[10] and Derry et al.[11], in which over 1000 values obtained through various methods are tabulated. The low precision of ϕ_s has limited in-depth investigation into, for example, its dependence on temperature (T)[12,13], strain[14–18], or even on gravity; see Cardona and Ley[1] and references therein.

While the primary concern may be the surface contamination, there is also a kinematic effect that can smooth the threshold of the electron emission seen in experiments[19,20]: Consider an ensemble of electrons each having just the energy to climb the potential barrier ϕ_s; it is only those directed normal to the surface that can indeed climb and be at rest on the outer surface. This illustrates that the number of electrons available on the outer surface diminishes when the threshold is approached. This effect was taken into account by Fowler to explain the rather smooth upturn of the photoyield when the photon energy $h\nu$ was swept across ϕ_s[19], and later, into all other emission techniques[21,22]. In the case for ultraviolet and X-ray photoemission spectroscopy (PES), the slow ends of the photoelectron spectra are observed as $\gtrsim$0.1-eV-wide slopes instead of step edges because of the effect[1,20], and the energy level of the slowest photoelectrons (E_s) has to be read from the point where the slope merges into the background (Fig. 1a). As a result, the values of ϕ_s are read typically with two to three significant digits[23–25] while the number of four does exist in some studies[1,26]. In any case, the degree of certainty is lower than the sub-meV precision routinely attained when setting the energy level of the Fermi cutoff (E_f) located on the fast end of the spectrum[27,28].

The kinematic effect upon the emission[19,20] strongly indicates that, in order to select out the slowest electron among the emitted electrons, not only their energy but also their trajectory has to be resolved. Here, we apply angle-resolved PES (ARPES) to the slow photoelectrons emitted from a crystal surface of a metal. As will be explained in the present study, the slowest end seen in ARPES becomes a step edge (Fig. 1a) that is intrinsically sharper than the Fermi cutoff. Therefore, ARPES has the potential to locate E_s with the degree of certainty much higher than that for locating E_f. This underlies the precise extraction of the work function via ARPES through the relationship $\phi_s = h\nu - (E_f - E_s)$. Simple though it may seem, the precise detection via ARPES was aided by the use of a fibre-laser-based light source[29] whose beam can be aligned and focused to take control over the trajectory of the slow photoelectrons in ARPES setups[30]; see the subsequent section, Laser-ARPES setup for slow photoelectrons. The slow end of the photoelectron distribution seen in fibre-laser ARPES retained the sharpness expected in Einstein's theory[31] and allowed us to monitor the work function with sub-meV precision.

Results

Laser-ARPES setup for slow photoelectrons. Slow photoelectrons are vulnerable to fields and their trajectories can easily be bent by the electric and magnetic fields remaining in the spectrometer[24]. Particularly, the slowest photoelectrons are those that have once been at rest on the outer surface, and taking control of their trajectory from the surface to the electron analyser is the most difficult. As will be explained later, the genuine cutoff of the slowest end seen in ARPES should exhibit the following two features (Fig. 1a). (1) The slow-side cutoff shows a parabolic angular dispersion. (2) The cutoff is a step edge whose width is not broadened by Fermi-Dirac distribution nor by the bandwidth of light. We set these two features, which were not described in the previous studies of the work function[1,32], as the criteria for the successful ARPES on the slow photoelectrons.

The technical difficulty to perform reliable ARPES on slow photoelectrons is gradually being removed, and currently, slow photoelectrons of $\lesssim$1 eV kinetic energy can be passed through modern electron analysers in a controlled trajectory. This advance has partly been propelled by the advent of low-$h\nu$ sources of $\lesssim$10 eV based on lasers[27,30,33–35], wherein the detection of slow photoelectrons becomes a mandatory. To attain a fair angular resolution particularly when the photoelectrons are slow, it is requested to keep the beam diameter less than 0.3 mm at the focal point of the electron lens (e-lens) attached to the analyser, and the laser-based sources can easily meet this demand.

We set up a fibre-laser-based source of $h\nu = 5.988$ eV[29] and docked it to an ARPES spectrometer equipped with a helium lamp (Fig. 1b; also see Supplementary Note 1 and Supplementary Fig. S1). The beam diameter at the focal point of the e-lens was set to ~0.1 mm through a procedure that utilises a pin hole[30]. The oscillator of the fibre-laser source was stably mode locked for at least three months, which ensures that the profile of the laser such as the photon energy and band width was locked during the measurements. While fibre-laser ARPES was used to detect the slow photoelectrons, helium-lamp ARPES was also used to characterise the band dispersions and to calibrate the photoelectron energy $E_{PE} - E_F$ referenced to the Fermi level of the sample in electrical contact to the analyser; see 'Methods'.

Preparation of Au(111). As a model system, we investigated the (111) surface of gold. Gold is a noble metal and is an exemplary metal for electrodes. Studies of the work function of gold begun partly in pursuit of a reference standard[36,37], and the values for Au(111) have been found to be in 5.2–5.6 eV[10,11,25,38]. It is well known that the work function is sensitive to the surface quality at the atomic level, and there is consensus that the cleaner the surface is, the higher the work function is, especially for materials with the values greater than ~4 eV[39]. We prepared two samples of Au(111) (samples 1 and 2) through cycles of Ar-ion bombardment and annealing ('Methods'). The dispersion of the Shockley surface state formed on Au(111)[40–42] was observed by using helium-lamp ARPES (Fig. 1c). The band dispersion for sample 2 was slightly sharper than that for sample 1 (Supplementary Fig. S2 and Supplementary Note 2). As we shall see later, sample 2 indeed exhibited higher ϕ_s than that of sample 1.

Slow end seen with fibre-laser ARPES. The panels in Fig. 2a–d show the photoelectron distributions obtained when Au(111) of sample 1 was illuminated by the fibre-laser source. The fastest photoelectrons formed the Fermi cutoff at the known photon energy 5.988 eV of the source, which ensures the accuracy of $E_{PE} - E_F$ calibrated by using the He Iα line. As the sample was rotated from $R = 0$ (Fig. 2a; normal-emission configuration) to 7.5° (Fig. 2d), the Shockley surface band became fully visible up to the Fermi cutoff. However, the bottom of the band was truncated by the cutoff on the slow side because the electrons excited from the bottom could not overcome the work function. The visibility of the Shockley band down to the cutoff provides a credit that our

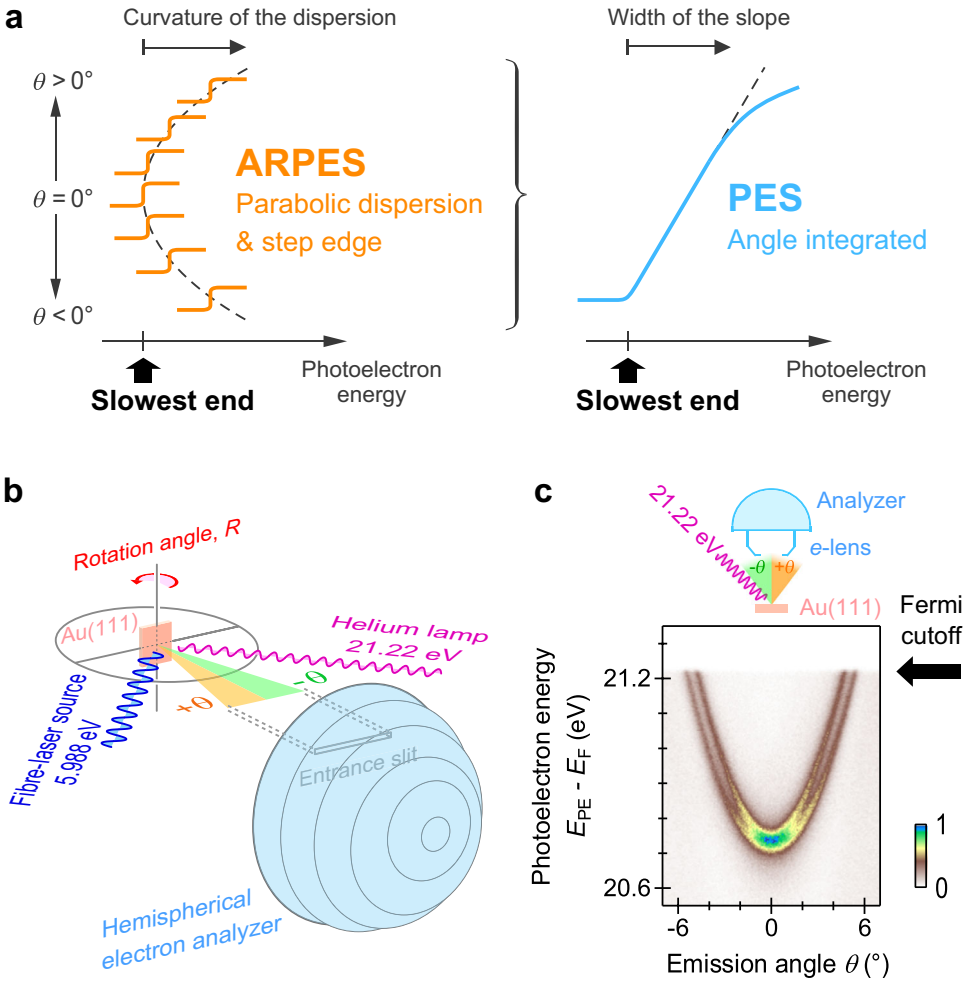

Fig. 1 Detecting the slow photoelectrons. a Slow photoelectrons seen via photoemission spectroscopy (PES) and angle-resolved PES (ARPES). θ is the emission angle. When integrated over a certain emission anglular cone about the normal emission ($\theta = 0°$), the spectrum becomes sloped. **b** The ARPES setup equipped with a fibre-laser source and a helium lamp. Au(111) is held at 30 K unless described otherwise. The sample and entrance of the e-lens are electrically connected to the common ground. **c** Shockley state of sample 1 seen with helium-lamp ARPES. The state is dispersing in the plane spanned by the photoelectron energy $E_{PE} - E_F$ and θ, where E_{PE} and E_F are the photoelectron energy level and Fermi level, respectively.

ARPES setup was operating agreeably for the slowest photoelectrons even without applying any bias voltage on the sample; also see Supplementary Fig. S2 and Supplementary Note 2.

Our main observations for Fig. 2a–d are of the slow side cutoff. First, the cutoff energy depended on the emission angle of the photoelectrons (θ) and exhibited a parabolic dispersion bottomed at the surface normal, $\theta = 0°$. Second, the slow-side cutoff was a sharp step edge in contrast to the $\gtrsim$0.1-eV-wide slopes observed in ultraviolet and X-ray PES[23–26]. The parabolic cutoff is distinct from the parabolic boundary that occurs in the photoelectron distribution mapped onto energy–momentum (E–k) plane. As is well known, the mapping function[43] has a range that sets a parabolic boundary in E–k plane whose bottom occurs not in the surface normal but in the direction towards the e-lens. Such a boundary in E–k plane can be seen for example in Bovet et al.[44] The cutoff herein is observed in E–θ plane and its bottom followed the surface normal when the sample was rotated from $R = 0$ to 7.5°. Therefore, the parabolic cutoff is intrinsic to the emission from the surface.

In order to quantify the sharp-and-parabolic cutoff, we performed a fitting procedure and extracted the energy and width of the cutoff as functions of θ. In the procedure, we first set a cutoff function (CF), which was a step distribution function of a linear slope convoluted with a Gaussian; for the explicit form of CF, see 'Methods'. Then, with the CF, we fitted the energy distribution curves (EDCs) of the data shown in Fig. 2a–d. The case for the $R = 0°$ distribution is presented in Fig. 2e. The four parabolic curves nicely overlapped each other (Fig. 2f) and the full width at half maximum of the Gaussian (FWHM: γ) was averaged as $\gamma = 10.8 \pm 3.4$ meV (Fig. 2g). The cutoff energy around $\theta = \pm 0.5°$, in which there are 115 data points, was averaged as 5.5034 eV with one standard deviation of $\sigma = 1.2$ meV (inset to Fig. 2f). The energy at the bottom of the parabolic cutoff will subsequently be identified as the absolute value of the work function. Note, the overlap of the four dispersions seen in Fig. 2f shows that the dispersion shifted with the known interval of 2.5° along the emission angle axis and ensures the angular scaling of θ.

With the sharp cutoff as a measure, we were able to discern the aging of the surface. After keeping Au(111) of sample 1 in the spectrometer for 10 h, the sample surface became less clean and the cutoff shifted downwards; see, Supplementary Fig. S3 and Supplementary Note 3. The shift was as small as 5.5 meV and was attributed to the reduction in the work function due to residual gas weakly physisorbed on the surface. The reduction is consistent with the trend that the work function lowers as the surface becomes less clean[39]. There was no discernible shift of the Fermi cutoff during the 10 h, which indicated that the analyser condition was stable during the measurement; see 'Methods'.

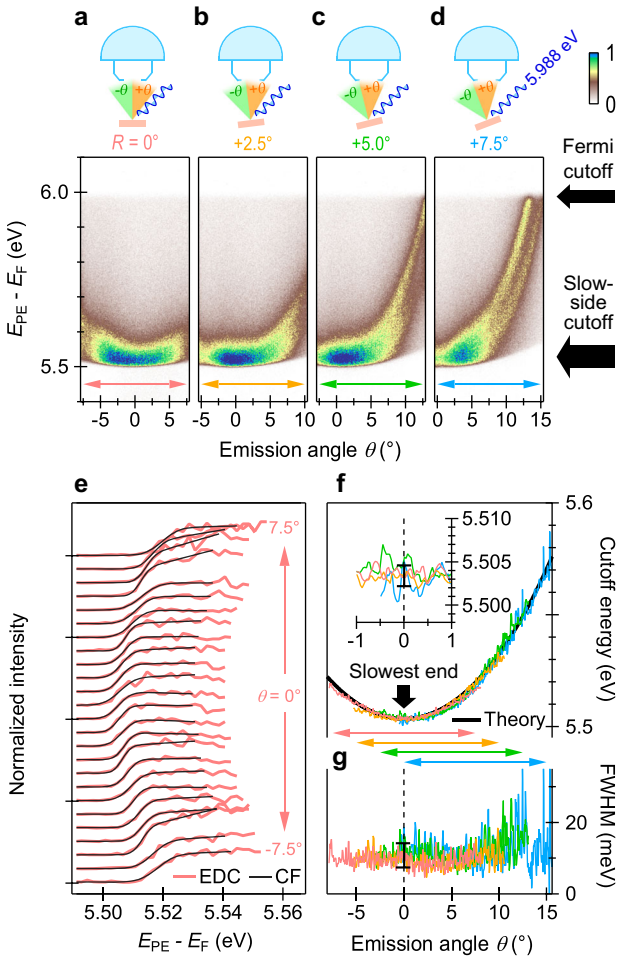

Fig. 2 Sharp and parabolic cutoff on the slow side. a–d Photoelectron distributions detected with fibre-laser angle-resolved photoemission spectroscopy. The sample was rotated from $R = 0$ (**a**) to 7.5° (**d**), where R is the rotation angle. The distributions are mapped in the plane spanned by the photoelectron energy ($E_{PE} - E_F$) and emission angle (θ), where E_{PE} and E_F are the photoelectron energy level and Fermi level, respectively. **e** Energy distribution curves (EDCs) and cutoff functions (CFs) around the cutoff acquired in the $R = 0°$ configuration. Cutoff energy (**f**) and width (**g**) of the CFs as functions of θ. The inset to **f** shows the cutoff energy around $\theta = 0°$, with the bar indicating 5.5034 ± 0.0012 eV for the values in [−0.5, 0.5°]. The bar in **g** indicates 10.8 ± 3.4 meV for the values in [−7.5, 15°].

In a separate run of the measurement on sample 2, we varied the temperature from 30 to 90 K and monitored the cutoff (Fig. 3a–c). In contrast to the Fermi cutoff, the slow-end cutoff remained sharp (Fig. 3d). The width of the slowest end around $\theta = \pm 0.5°$, in which there are 45 data points, was $\gamma = 8.3 \pm 1.0$ meV and the cutoff energy of the slowest end stayed at 5.5553 eV with one standard deviation of $\sigma = 0.4$ meV (Fig. 3e). That is to say, there was no temperature dependence in the work function with the precision of ± 0.4 meV/60 K $= \pm 0.08 k_B$, where k_B is the Boltzmann constant. The absolute value 5.5553 eV was higher than the value 5.5034 eV for sample 1 and is comparable to the highest reported work function of 5.6 ± 0.1 eV on Au(111) obtained through a Fowler plot[38]. Thus, with the work function as the measure[39], the surface quality of sample 2 was better than that of sample 1 and was comparable to that studied in Pescia and Meier[38].

Before explaining why the cutoff on the slow side appears sharp and parabolic, we point out that the cutoff is not only truncating the Shockley band but also the background signal, as clearly seen at $\theta > 10°$ in Fig. 2d. The background signal could originate from bulk bands as well as photoelectrons that have encountered some scattering[45]. This observation indicates that, when explaining the features of the cutoff, the photoelectrons forming the Shockley band and background signal have to be treated on equal footings. We thus consider a model for whatever photoelectrons that pass through a homogeneous surface characterised by a single work function ϕ_s. If there had been multiple edges in the spectrum[24], the surface would have been judged as non-uniform, or patchy[12,24].

Trajectory of the threshold photoelectrons. The sharp-and-parabolic appearance of the cutoff can be understood by considering the trajectory of 'threshold photoelectrons'. Below, we first explain the photoelectron refraction, or the kinematic constraints upon the emission across the surface[1,19,20], and define the threshold photoelectrons. Then, we consider their trajectories from the surface to the entrance of the e-lens that collects the photoelectrons into the hemispherical analyser.

When passing through the surface, photoelectrons are refracted because the work function acts as a potential barrier. As shown in Fig. 4a, the angle of refraction becomes large as the angle of incidence increases, and at a critical angle, the photoelectrons travel tangential to surface. We call these tangential photoelectrons the threshold photoelectrons. Their kinetic energy on the surface is $\varepsilon_s^{th} = (\hbar \mathbf{k}_s^{th})^2/2m \geq 0$, where m is the electron mass and $\hbar \mathbf{k}_s^{th}$ is the momentum that is parallel to the surface by definition. The energy level of a threshold photoelectron E_{PE}^{th} can be described as (Fig. 4b),

$$E_{PE}^{th} = E_F + \phi_s + \varepsilon_s^{th} \geq E_F + \phi_s \equiv V_{vac}^{z_s}, \quad (1)$$

where $V_{vac}^{z_s}$ is the vacuum level just outside the surface.

The threshold photoelectrons cannot reach the e-lens as long as they are travelling tangential to the surface. Here, we are reminded that, even when the sample and e-lens are electrically connected, electric fields can exist between the two; see Fig. 4b. The vacuum level is a solution to the Poisson equation, $\nabla^2 V_{vac}(\mathbf{r}) = 0$, with the boundary condition set by the work function on the vacuum boundary. Thus, V_{vac} differs by $\Delta\phi = \phi_s - \phi_a$ between the sample and entrance of the e-lens, where ϕ_a is the work function of the material that coats the interior of the e-lens and analyser. When $\Delta\phi > 0$, the threshold photoelectrons can take off the surface and be dragged towards the e-lens. Their kinetic energy at the e-lens entrance becomes $\varepsilon_a^{th} = \varepsilon_s^{th} + \Delta\phi$ (Fig. 4b). For the case when $\Delta\phi < 0$, see later.

Analytic solutions for the trajectory exist when we can regard the electric field to be directed along the surface normal (z) (Fig. 4c). This arrangement is similar to an infinitely large parallel-plate capacitor, but each plate is made of different materials. Then, while dragged, the momentum parallel to the surface is unchanged. At the e-lens entrance, the momentum along z ($\hbar k_a^{\perp}$) can be obtained through $(\hbar k_a^{\perp})^2/2m = \Delta\phi$, and the nominal emission angle (θ) seen by the analyser becomes $\tan\theta = |\mathbf{k}_s^{th}|/k_a^{\perp}$ (Fig. 4c). Thus, equation (1) can be described as

$$E_{PE}^{th} - E_F = \phi_s + \Delta\phi \tan^2\theta. \quad (2)$$

Equation (2) illustrates that, when entering the e-lens, the energy of the threshold photoelectron exhibits a parabolic angular dispersion, and this is the dispersion detected by the analyser. In Fig. 2f, we overlaid the curve of equation (2) with $\Delta\phi = 0.9$ eV, which determines the curvature, and the bottom of the dispersion $\phi_s = 5.5034 \pm 0.0012$ eV is identified as the absolute value of the work function.

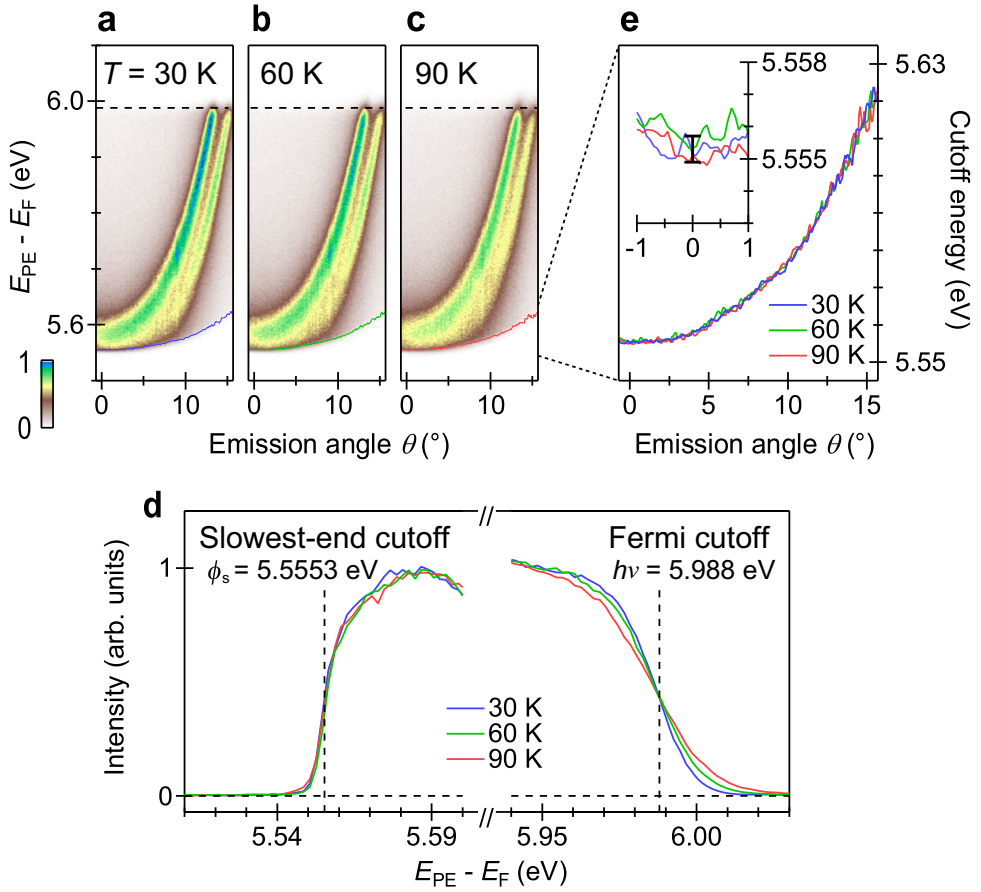

Fig. 3 Temperature dependence of the cutoff. Photoelectron distributions recorded at the temperatures of 30 (**a**), 60 (**b**) and 90 K (**c**) on sample 2. The distributions are mapped in the plane spanned by the photoelectron energy ($E_{PE} - E_F$) and emission angle (θ), where E_{PE} and E_F are the photoelectron energy level and Fermi level, respectively. **d** Temperature dependence of the distribution curves across the slowest-end cutoff at $\theta = 0°$ and across the Fermi cutoff. ϕ_s is the work function of the sample. **e** The slow-side cutoffs at various temperatures. Inset shows the expanded view around the emission angle $\theta = 0°$, in which one standard deviation σ of 0.4 meV for the values in [−0.5, 0.5°] is indicated by an error bar.

For completeness, we present the dispersion of the angle-resolved cutoff when the sample is applied with negative bias voltage $-\nu/e$ with respect to the analyser:

$$E_{PE}^{th} - E_F = \phi_s + \nu + (\Delta\phi + \nu)\tan^2\theta. \quad (3)$$

Here, $E_F + \nu$ becomes the Fermi level of the sample. When $\Delta\phi + \nu > 0$, the threshold photoelectrons are dragged towards the *e*-lens and the intrinsic cutoff becomes visible. With increasing ν, the dispersion shifts upwards in energy and its curvature (prefactor of $\tan^2\theta$) is increased. The increase of the curvature is in accordance to the photoelectron acceptance cone being tunable with ν[46,47]. At $\nu \gtrsim 25$ eV, the lowering of the work function due to the Schottky effect[12] can exceed 1 meV and may prevail when seen with the sub-meV precision; see 'Methods'. When integrated over a certain anglular cone about the normal emission, the cutoff is smoothed into a slope (Fig. 1a right schematic) as seen in ultraviolet and X-ray PES[23–26]. This slope seen in the normal-emission configuration is the lineshape formulated in Cardona and Ley[1] and in Krolikowski and Spicer[20] that took the Fowler effect into account, although the role of $\Delta\phi$ was not explicated. According to Eq. (3), the width of the slope in the integrated spectrum becomes wider as ν is increased, while the angle-resolved cutoff remains sharp; see Fig. 1a for the relationship between the curvature seen in ARPES and width of the sloped region seen in PES.

The demonstration of the sub-meV precision measurement under the biased condition is presented in Supplementary Fig. S4: We performed the measurement at room temperature and at the pressure of 6×10^{-10} Torr on the surface of an exfoliated highly-oriented pyrolitic graphite[29]. The width of the slowest-end cutoff was as narrow as $\gamma = 8.0$ meV when one battery of $\nu/e = 1.62$ V was attached, and the energy of the slowest end around $\theta = \pm 0.5°$ was leveled within one standard deviation of $\sigma = 0.15$ meV when the number of the attached batteries was varied from one to four. For the details of the demonstration, see Supplementary Note 4.

On the role of the monochromaticity. It was shown in the previous section that the parabolic dispersion of the slow-end cutoff depends solely on how the threshold photoelectrons were dragged from the outer surface to the *e*-lens; it does not depend on how the threshold photoelectrons were generated. Whatever the value of $h\nu$ may be, the threshold photoelectrons emerged on the outer surface line up on the identical dispersion when entering the *e*-lens. This point is implicit in Eqs. (1)–(3) as well as the definition of the work function $\phi_s = E_s - E_F$ being independent of $h\nu$. Thus, the cutoff on the slow end is not blurred by the bandwidth of light ($\gamma_{h\nu}$) besides not being affected by the temperature dependence of the Fermi-Dirac function. Therefore, the cutoff can be observed with the resolution (γ_a) set by the analyser and the stability of the bias voltage. This point is in strong contrast to the bands and Fermi cutoffs seen with the convoluted resolution $(\gamma_a^2 + \gamma_{h\nu}^2)^{1/2}$. The width of the slow-end cutoff being slightly larger for sample 1 (10.8 ± 3.4 meV) than that for sample 2 (8.3 ± 1.0 meV) can be attributed to the degree

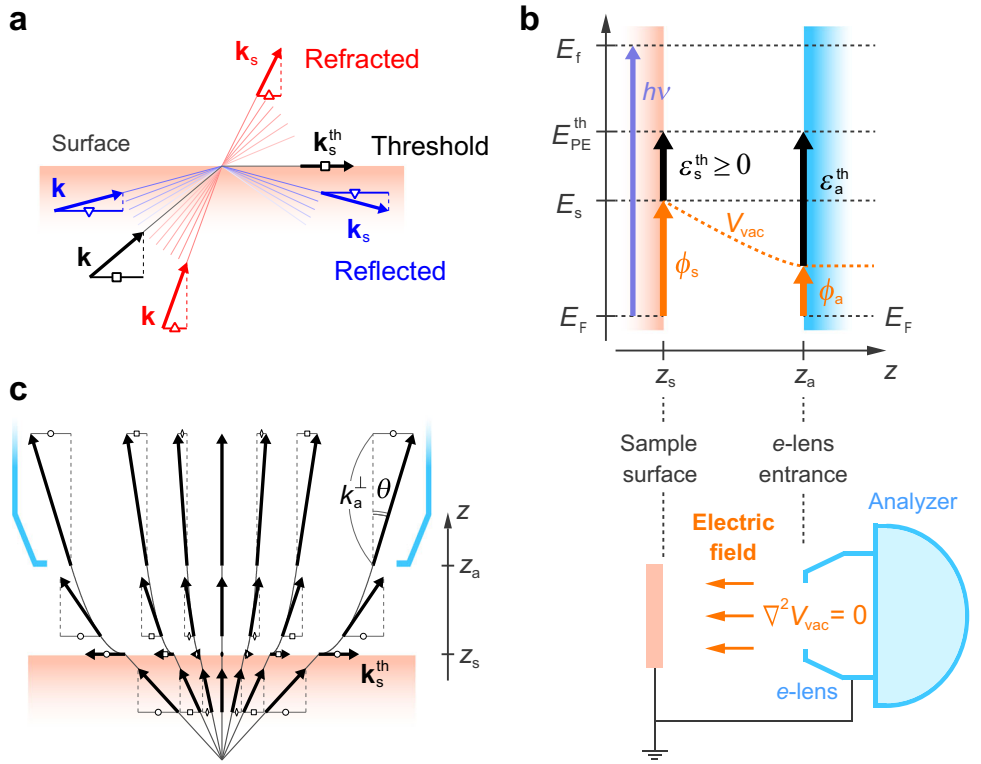

Fig. 4 Trajectory of the threshold photoelectrons. a The refraction and reflection of the photoelectrons and the definition of the threshold photoelectrons. Red, blue and black lines indicate the trajectory of the electrons. **k** is the photoelectron momentum before incident on the surface; $\mathbf{k}_s$ and $\mathbf{k}_s^{th}$ are those after the incidence. **b** The energy diagram for the threshold photoelectrons. E_f, E_{PE}^{th} and E_s are the energy levels of the fastest, threshold and slowest photoelectron, respectively, and E_F is the Fermi level. ϕ_s and ϕ_a are the work functions of the sample and analyser, respectively. The lower section shows the electric field existing between the sample and *e*-lens separated with the working distance of $z_a - z_s \sim 32$ mm (Supplementary Note 1), where z_s and z_a are the locus of the sample surface and *e*-lens entrance on the *z* axis, respectively. The vacuum level (V_{vac}) is the solution to the Poisson equation. ε_s^{th} and ε_a^{th} are the kinetic energy of the threshold photoelectron at $z = z_s$ and z_a, respectively. **c** The trajectory (black lines) of the threshold photoelectrons dragged by the electric field. The threshold photoelectron emitted normal to the surface has the smallest momentum (shortest black arrow) when entering the *e*-lens, and hence, is the slowest and forms the slowest-end cutoff. $k_a^{\perp}$ is the *z* component of the threshold-photoelectron momentum at $z = z_a$ and θ is the emission angle seen by the analyser.

of inhomogeneity of the work function (γ_ϕ) within the probed area set by the ~0.1-mm beam size. That is to say, the width of the cutoff seen in ARPES is $\gamma = (\gamma_a^2 + \gamma_\phi^2)^{1/2}$. When $\gamma_\phi \to 0$, the width γ becomes the direct measure of γ_a.

The only but important role for the light to be monochromatic was to precisely locate the energy level of the Fermi cutoff E_f, which was the requisite to refer to the absolute value of the work function[1,23]; see 'Methods'. If the purpose was only to observe the parabolic cutoff and monitor the relative value of the work function, the monochromaticity of the source is not needed; whatever sources that can generate an ensemble of excited electrons in the crystal, or an ensemble of threshold photoelectrons travelling along the outer surface, can be utilised. For example, synchrotron light can be used[32] even when its photon energy is drifting; intense femtosecond infra-red pulses that can generate muti-photon photoelectrons can be used[48,49] provided that the intense field of the pulse does not significantly alter the work function[12]; deuterium lamps and electron guns, the latter in the setup of momentum-resolved electron-energy loss spectroscopy[50,51], may also be used if the beam size can be reduced sufficiently.

Discussion

In summary, we applied 6-eV fibre-laser ARPES to a model system Au(111) and investigated the trajectory of the slow photoelectrons that marginally overcame the work function. The slow end of the photoelectron distribution was successfully detected. It showed a parabolic angular distribution bottomed at normal emission. Moreover, the cutoff was a step edge and was sharper than the Fermi cutoff. A kinematic model described the sharp-and-parabolic cutoff as follows: The bottom of the dispersion is the cutoff formed by the slowest photoelectrons; the curvature of the dispersion depends on the slope of the vacuum level across the sample and *e*-lens; the cutoff is a step edge whose sharpness is indifferent to the bandwidth of light. Thereby, we derived the work function with one standard deviation as small as $\sigma = 0.4$ meV and demonstrated the potential of ARPES that is intrinsically free from the Fowler effect.

Because the work function is sensitive to the surface quality at the atomic level[1,4,12,39], it is practically impossible to obtain the accurate value of ϕ_s of an ideal crystal surface that has no contamination. In this sense, the present contribution just adds two more values to the literature, namely $\phi_s = 5.5034 \pm 0.0012$ and 5.5553 ± 0.0004 eV for the studied surfaces of Au(111). However, the significance is in their precision[10,11]. This owes to the capability of ARPES to resolve the direction of the emission, which was the prerequisite to observe the spectral cutoff formed only by the slowest photoelectrons emitted along the surface normal. We demonstrated that the temperature dependence is as small as $d\phi_s/dT < \pm 0.08 k_B$ (Fig. 3), which puts strong constraints on the theory that typically predicts $d\phi_s/dT = \mathcal{O}(k_B)$[12,13], and suggests that

there can be a compensation between the bulk and surface contributions to $d\phi_s/dT$ for Au(111)[13]. The precision also allowed us to discern the surface aging over 10 hours as the 5.5-meV shift of the work function (Supplementary Fig. S3). The precise measurement by using ARPES can open new opportunities to monitor the work function on the surface, for example, in ambient conditions[52–55], under controlled application of strain[56,57], during phase transitions or crossovers[58–60] and upon irradiation of intense femtosecond pulses[30,61–64].

Methods

ARPES setup on Au(111). The Au(111) surface of ~1 × 1 cm^2 was prepared by repeating 1.8-keV Ar-ion sputtering and 550-K annealing on a single crystal of gold. The temperature on the surface during the annealing was monitored by a pyrometer whose emissivity was set to 0.05. The pressure during the final 10-min annealing of samples 1 and 2 were <7 × 10^{-10} and 4 × 10^{-10} Torr, respectively. After the annealing, the sample was cooled at a rate of ~15 K/min down to 400 K and then transferred to an ARPES chamber at a pressure of 3.7 × 10^{-11} Torr. A homemade light source based on optical fibres doped with ytterbium (Yb)[29,65,66] was docked to the chamber equipped with a hemispherical analyser (Scienta-Omicron, DA30-L), a retractable helium lamp, a six-axis manipulator, and a temperature controlled cryostat. The analyser had a one-dimensional entrance slit as illustrated in Fig. 1a, and photoelectrons directed into the slit were detected at once. The ARPES dataset was thus obtained as a two-dimensional matrix spanned by energy and emission angle. The wattage of the 5.988-eV probe light was ~1 μW. For details of the fibre-laser source, see Supplementary Note 1. The temperature of the sample was controlled in the range of 30–90 K. The degassing from the cryostat was below the detection limit of an ion gauge, whose read of the pressure did not vary during the temperature variation; see Supplementary Fig. S3e.

Energy reference for extracting the work function. As is well established (for example, see Park et al.[23]), the absolute value of the work function ϕ_s can be obtained by using photoemission spectroscopy, which owes to the working principle of the hemispherical analyser, or electrostatic deflection analysers in general, when used in a constant pass-energy mode[1]. Then, the photoelectron energy level (E_{PE}) can be referenced to E_F of the sample in electrical contact to the analyser without any other inputs except the photon energy ($h\nu$) of the source[23]. In the present study, the spectrum was recorded by sweeping the retardation voltage (v_r/e) applied in the e-lens section while setting the pass energy of the hemispherical analyser to 2 eV. The photoelectron energy $\varepsilon \equiv E_{PE} - E_F$ was calibrated as follows: We performed helium-lamp ARPES on gold evaporated on a sample holder at $T = 10$ K, and the value of the retardation voltage v_r^F/e at which the photoelectron excited from E_F passed through the hemisphere was determined from the Fermi cutoff, as routinely performed in ARPES studies[27,28]; then, the reference of ε was taken so that the cutoff appeared at the photon energy of the He Iα line (21.2180 eV). Note, whatever the sample's work function may be, the photoelectrons excited from E_F pass through the analyser when v_r matches the identified v_r^F/e, provided that the condition of the analyser such as the work function ϕ_a of the material that coats the interior of the e-lens and analyser is not changed during the measurement. When the spectra are displayed as functions of ε, the cutoff energy of the slowest end becomes the absolute value of the work function, whereas the Fermi cutoff appears at the photon energy of the source. We reiterate here that there is no need to know the absolute value of the analyser's work function ϕ_a, only its stability, for calibrating ε and for reading the absolute value of the sample's work function ϕ_s from the spectrum.

Fitting procedure for the cutoffs. The cutoff energy ε_s^{th} and width of the cutoff on the slow side were extracted by fitting the EDC at each emission angle with the step-edge-type cutoff function CF: $\int S(\varepsilon')\,\Theta(\varepsilon' - \varepsilon_s^{th})G(\varepsilon - \varepsilon'; \gamma)d\varepsilon'$. Here, $\Theta(\varepsilon)$ is a step function which is unity when $\varepsilon > 0$ but is zero otherwize, $G(\varepsilon; \gamma)$ is a Gaussian, γ is the FWHM of the Gaussian, and $S(\varepsilon)$ is the spectrum to be cut off and is represented by a linear slope, or the Taylor expansion up to the first order about the cutoff energy ε_s^{th}.

Estimation of the Schottky effect. All the spectra were taken with the sample and analyser electrically connected to common ground. Therefore, the lowering of the work function due to the Schottky effect $\Delta\phi_s = -(e^3E/4\pi\varepsilon_0)^{1/2}$ (see Fig. 1 of Herring and Nichols[12]) was at most caused by the residual electric field $E \sim \Delta\phi/e(z_a - z_s)$ (Fig. 4b). Here, ε_0 is the vacuum permittivity and $z_a - z_s \sim 32$ mm is the working distance between the sample surface and entrance of the e-lens (Supplementary Note 1). Inserting $\Delta\phi = 0.9$ eV obtained from the curvature of the parabolic cutoff (main text), $\Delta\phi_s \sim 0.2$ meV, which is smaller than the standard deviation of the found values of ϕ_s (main text). When a negative bias voltage $-v/e$ is applied to the sample, then $E \sim (\Delta\phi + v)/e(z_a - z_s)$, and $\Delta\phi_s$ can exceed 1 meV at $v \gtrsim 25$ eV.

Data availability

The authors declare that the data supporting the findings of this study are included within the paper and available from the corresponding author on reasonable request.

Code availability

Code used for the fitting procedure is available on reasonable request from the corresponding author.

Received: 9 January 2020; Accepted: 21 August 2020;
Published online: 11 September 2020

References

1. Cardona, M. & Ley, L. (eds) Photoemission in Solids (Springer-Verlag, Berlin, 1978).
2. Kahn, A. Fermi level, work function and vacuum level. *Mater. Horiz.* **3**, 7–10 (2016).
3. Bardeen, J. Theory of the work function. II. The surface double layer. *Phys. Rev.* **49**, 653–663 (1936).
4. Smoluchowski, R. Anisotropy of the electronic work function of metals. *Phys. Rev.* **60**, 661–674 (1941).
5. Lang, N. D. & Kohn, W. Theory of metal surfaces: work function. *Phys. Rev. B* **3**, 1215–1223 (1971).
6. Leung, T. C., Kao, C. L., Su, W. S., Feng, Y. J. & Chan, C. T. Relationship between surface dipole, work function and charge transfer: Some exceptions to an established rule. *Phys. Rev. B* **68**, 195408 (2003).
7. Vayenas, C. G., Bebelis, S. & Ladas, S. Dependence of catalytic rates on catalyst work function. *Nature* **343**, 625–627 (1990).
8. Ma, H., Yip, H. L., Huang, F. & Jen, A. K. Y. Interface engineering for organic electronics. *Adv. Funct. Mater.* **20**, 1371–1388 (2010).
9. Greiner, M. T. & Lu, Z.-H. Thin-film metal oxides in organic semiconductor devices: Their electronic structures, work functions and interfaces. *NPG Asia Mater.* **256**, e55 (2013).
10. Kawano, H. Effective work functions for ionic and electronic emissions from mono- and polycrystalline surfaces. *Prog. Surf. Sci.* **83**, 1–165 (2008).
11. Derry, G. N., Kern, M. E. & Worth, E. H. Recommended values of clean metal surface work functions. *J. Vac. Sci. Technol. A* **33**, 060801 (2015).
12. Herring, C. & Nichols, M. H. Thermonic emission. *Rev. Mod. Phys.* **119**, 185–270 (1949).
13. Kiejna, A. On the temperature dependence of the work function. *Surf. Sci.* **178**, 349–358 (1986).
14. Sekiba, D. et al. Strain-induced change in electronic structure of Cu(100). *Phys. Rev. B* **75**, 115404 (2007).
15. Wang, X. F., Li, W., Lin, J. G. & Xiao, Y. Electronic work function of the Cu (100) surface under different strain states. *EPL* **89**, 66004 (2010).
16. Peng, X., Tang, F. & Copple, A. Engineering the work function of armchair graphene nanoribbons using strain and functional species: a first principles study. *J. Phys.: Condens. Matter* **24**, 075501 (2012).
17. Lanzillo, N. A., Simbeck, A. J. & Nayak, S. K. Strain engineering the work function in monolayer metal dichalcogenides. *J. Phys.: Condens. Matter* **27**, 175501 (2015).
18. Wu, Y. et al. Strain effects on the work function of an organic semiconductor. *Nat. Commun.* **7**, 10270 (2016).
19. Fowler, R. H. The analysis of photoelectric sensitivity curves for clean metals at various temperatures. *Phys. Rev.* **38**, 45–56 (1931).
20. Krolikowski, W. F. & Spicer, W. E. Photoemission studies of the noble metals. I. Copper. *Phys. Rev.* **185**, 882–900 (1969).
21. DuBridge, L. A. Theory of the energy distribution of photoelectrons. *Phys. Rev.* **43**, 727–741 (1933).
22. Jensen, K. L. General formulation of thermal, field, and photoinduced electron emission. *J. Appl. Phys.* **102**, 024911 (2007).
23. Park, Y., Choong, V., Gao, Y., Hsieh, B. R. & Tang, C. W. Work function of indium tin oxide transparent conductor measured by photoelectron spectroscopy. *Appl. Phys. Lett.* **68**, 2699–2701 (1996).
24. Helander, M. G., Greiner, M. T., Wang, Z. B. & Lu, Z. H. Pitfalls in measuring work function using photoelectron spectroscopy. *Appl. Surf. Sci.* **256**, 2602–2605 (2010).
25. Akaike, K., Koch, N. & Oehzelt, M. Fermi level pinning induced electrostatic fields and band bending at organic heterojunctions. *Appl. Phys. Lett.* **105**, 223303 (2014).
26. Koitaya, T., Shimizu, S., Mukai, K., Yoshimoto, S. & Yoshinobu, J. Kinetic and geometric isotope effects originating from different adsorption potential energy surfaces: cyclohexane on Rh(111). *J. Chem. Phys.* **136**, 214705 (2012).
27. Okazaki, K. et al. Octet-line node structure of superconducting order parameter in KFe_2As_2. *Science* **337**, 1314–1317 (2012).

28. Huang, J. et al. High precision determination of the Planck constant by modern photoemission spectroscopy. *Rev. Sci. Instrum.* **91**, 045116 (2020).
29. Ishida, Y. et al. High repetition pump-and-probe photoemission spectroscopy based on a compact fiber laser system. *Rev. Sci. Instrum.* **87**, 123902 (2016).
30. Ishida, Y. et al. Time-resolved photoemission apparatus achieving sub-20-meV energy resolution and high stability. *Rev. Sci. Instrum.* **85**, 123904 (2014).
31. Einstein, A. Concerning an heuristic point of view toward the emission and transformation of light. *Ann. Phys.* **75**, 132–148 (1905).
32. Paggel, J. J. et al. Atomic-layer-resolved quantum oscillations in the work function: theory and experiment for Ag(100). *Phys. Rev. B* **66**, 233403 (2002).
33. Koralek, J. D. et al. Laser based angle-resolved photoemission, the sudden approximation, and quasiparticle-like spectral peaks in $Bi_2Sr_2CaCu_2O_{8+\delta}$. *Phys. Rev. Lett.* **96**, 017005 (2006).
34. Harter, J. W. et al. A tunable low-energy photon source for high-resolution angle-resolved photoemission spectroscopy. *Rev. Sci. Instrum.* **83**, 113103 (2012).
35. Zhou, X. et al. New developments in laser-based photoemission spectroscopy and its scientific applications: a key issues review. *Rep. Prog. Phys.* **81**, 062101 (2018).
36. Huber, E. E. The effect of mercury contamination on the work function of gold. *Appl. Phys. Lett.* **8**, 169–171 (1966).
37. Rivière, J. C. The work function of gold. *Appl. Phys. Lett.* **8**, 172 (1966).
38. Pescia, D. & Meier, F. Spin polarized photoemission from gold using circularly polarized light. *Surf. Sci.* **117**, 302–309 (1982).
39. Eastman, D. E. Photoelectric work functions of transition, rare-earth, and noble metals. *Phys. Rev. B* **2**, 1–2 (1970).
40. LaShell, S., McDougall, B. A. & Jensen, E. Spin splitting of an Au(111) surface state band observed with angle resolved photoelectron spectroscopy. *Phys. Rev. Lett.* **77**, 3419–3422 (1996).
41. Hoesch, M. et al. Spin structure of the shockley surface state on Au(111). *Phys. Rev. B* **69**, 241401 (2004).
42. Kim, B. et al. Spin and orbital angular momentum structure of Cu(111) and Au(111) surface states. *Phys. Rev. B* **85**, 195402 (2012).
43. Ishida, Y. & Shin, S. Functions to map photoelectron distributions in a variety of setups in angle-resolved photoemission spectroscopy. *Rev. Sci. Instrum.* **89**, 043903 (2018).
44. Bovet, M. et al. Excited states mapped by secondary photoemission. *Phys. Rev. Lett.* **93**, 107601 (2004).
45. Strocov, V. N. Intrinsic accuracy in 3-dimensional photoemission band mapping. *J. Electron Spectrosc. Relat. Phenom.* **130**, 65–78 (2003).
46. Tusche, C., Krasyuk, A. & Kirschner, J. Spin resolved bandstructure imaging with a high resolution momentum microscope. *Ultramicroscopy* **159**, 520–529 (2015).
47. Yamane, H. et al. Acceptance-cone-tunable electron spectrometer for highly-efficient constant energy mapping. *Rev. Sci. Instrum.* **90**, 093102 (2019).
48. Aeschlimann, M. et al. Observation of surface enhanced multiphoton photoemission from metal surfaces in the short pulse limit. *J. Chem. Phys.* **102**, 8606–8613 (1995).
49. Bisio, F., Nývlt, M., Franta, J., Petek, H. & Kirschner, J. Mechanisms of high-order perturbative photoemission from Cu(001). *Phys. Rev. Lett.* **96**, 087601 (2006).
50. Zhu, X. et al. High resolution electron energy loss spectroscopy with two-dimensional energy and momentum mapping. *Rev. Sci. Instrum.* **86**, 083902 (2015).
51. Kogar, A. et al. Signatures of exciton condensation in a transition metal dichalcogenide. *Science* **358**, 1314–1317 (2018).
52. Reuter, K. & Scheffler, M. First-principles atomistic thermodynamics for oxidation catalysis: surface phase diagrams and catalytically interesting regions. *Phys. Rev. Lett.* **90**, 046103 (2003).
53. Grass, M. E. et al. New ambient pressure photoemission endstation at Advanced Light Source beamline 9.3.2. *Rev. Sci. Instrum.* **81**, 053106 (2010).
54. Takagi, Y. et al. X-ray photoelectron spectroscopy under real ambient pressure conditions. *Appl. Phys. Express* **10**, 076603 (2017).
55. Amann, P. et al. A high-pressure x-ray photoelectron spectroscopy instrument for studies of industrially relevant catalytic reactions at pressures of several bars. *Rev. Sci. Instrum.* **90**, 103102 (2019).
56. Pfau, H. et al. Detailed band structure of twinned and detwinned $BaFe_2As_2$ studied with angle-resolved photoemission spectroscopy. *Phys. Rev. B* **99**, 035118 (2019).
57. Sunko, V. et al. Direct observation of a uniaxial stress-driven Lifshitz transition in Sr_2RuO_4. *npj Quantum Mater.* **4**, 46 (2019).
58. Rietveld, G., Chen, N. Y. & van der Marel, D. Anomalous temperature dependence of the work function in $YBa_2Cu_3O_{7-\delta}$. *Phys. Rev. Lett.* **69**, 2578–2581 (1992).
59. Fecher, G. H., Schmied, B. & Schönhense, G. Temperature-dependent ARUPS from the heavy fermion compound $CeNi_2Ge_2$(001). *J. Electron Spectrosc. Relat. Phenom.* **101–103**, 771–776 (1999).
60. Weber, A. P. et al. Spin-resolved electronic response to the phase transition in $MoTe_2$. *Phys. Rev. Lett.* **121**, 156401 (2018).
61. Fausti, D. et al. Light-induced superconductivity in a stripe-ordered cuprate. *Science* **331**, 189–191 (2011).
62. Kaiser, S. et al. Optically induced coherent transport far above T_c in underdoped $YBa_2Cu_3O_{6+\delta}$. *Phys. Rev. B* **89**, 184516 (2014).
63. Bovensiepen, U. & Kirchmann, P. S. Elementary relaxation processes investigated by femtosecond photoelectron spectroscopy of two-dimensional materials. *Laser Photonics Rev.* **6**, 589–606 (2012).
64. Miller, T. L., Zhang, W., Eisaki, H. & Lanzara, A. Particle-hole asymmetry in the cuprate pseudogap measured with time-resolved spectroscopy. *Phys. Rev. Lett.* **118**, 097001 (2017).
65. Zhou, X., Yoshitomi, D., Kobayashi, Y. & Torizuka, K. Generation of 28-fs pulses from a mode-locked ytterbium fiber oscillator. *Opt. Express* **16**, 7055–7059 (2008).
66. Nakamura, T., Tani, S., Ito, I. & Kobayashi, Y. Magneto-optic modulator for high bandwidth cavity length stabilization. *Opt. Express* **25**, 4994–5000 (2017).

Acknowledgements

Y.I., T.O. and Y.K. acknowledge T. Nakamura for standardising the so-called *N*-box designed for compacting and stabilising the Yb-doped fibre-laser oscillator. This work was conducted under the ISSP-CCES Collaborative Programme and was supported by the Institute for Basic Science in Republic of Korea (Grant Numbers IBS-R009-Y2 and IBS-R009-G2) and by JSPS KAKENHI (Grant Numbers 17K18749, 18H01148, 19K22140 and 19KK0350). Y.I. acknowledges the financial support by the University of Tokyo for the sabbatical stay at Seoul National University.

Author contributions

Y.I. conceived the project; Y.I. and T.O. set up the fibre-laser system under the supervision of Y.K.; J.K.J., M.S.K., J.K., Y.S.K. and I.S. maintained the ARPES system constructed at Seoul National University under the direction of C.K.; Y.I. prepared the sample with instructions from J.K.J. and I.S.; Y.I. performed ARPES measurements with support from J.K.J., M.S.K., J.K, Y.S.K. and D.C.; Y.I. analysed the data and wrote the manuscript with input from all authors.

Competing interests

The authors declare no competing interests.

Additional information

Supplementary information is available for this paper at https://doi.org/10.1038/s42005-020-00426-x.

Correspondence and requests for materials should be addressed to Y.I.

Reprints and permission information is available at http://www.nature.com/reprints

Publisher's note Springer Nature remains neutral with regard to jurisdictional claims in published maps and institutional affiliations.